Prediction of Turbulent Gas-Solid Flow in a Duct with a 90° Bend Using an Eulerian-Lagrangian Approach

Derrick O. Njobuenwu, Michael Fairweather, and Jun Yao
Institute of Particle Science and Engineering, School of Process, Environmental and Materials Engineering, University of Leeds, Leeds LS2 9JT, UK

DOI 10.1002/aic.12572
Published online March 4, 2011 in Wiley Online Library (wileyonlinelibrary.com).

A dilute, particle-laden turbulent flow in a square cross-sectioned duct with a 90° bend is modeled using a three-dimensional Eulerian-Lagrangian approach. Predictions are based on a second-moment turbulence closure, with particles simulated using a Lagrangian particle tracking technique, coupled to a particle-wall interaction algorithm and a random Fourier series method used to model particle dispersion. The performance of the model is tested for a gas-solid flow in a horizontal-to-vertical duct, with predictions showing good agreement with experimental data. In particular, the consistent use of anisotropic and fully three-dimensional approaches throughout yields predictions that result in fluctuating particle velocities in acceptable agreement with data. © 2011 American Institute of Chemical Engineers *AIChE J,* 58: 14–30, 2012
Keywords: gas-solid flow, duct, 90° bend, RANS, second-moment closure, Lagrangian particle tracking

Introduction

Gas-solid flows around bends of various cross sections and through other curved channels are of considerable importance in many industries. Bends and elbows are commonly used in many applications such as pneumatic conveyers and dryers, as well as in coal-fired power plant, food processing, the chemical industry, and for pollution control. In all these applications, there is a need for a detailed understanding of the particle-laden flow, and a requirement for predictive techniques that provide both qualitative and quantitative flow information, to permit the design and operation of efficient conveying systems. Of particular interest in relation to such flows are the turbulent dispersion of particles within the flow, the erosion by particles of any concave bend walls, particle deposition within the flow, and the formation of solid particle ropes downstream of a bend.

Correspondence concerning this article should be addressed to M. Fairweather at m.fairweather@leeds.ac.uk.

Previous work in relation to these complex flows has involved both physical and numerical modeling. However, there remains an interest in developing a better understanding of their behavior, and the various parameters, which influence them, as to date these are not sufficiently well understood to permit the development of predictive techniques that are usable in a general context. Early work on the prediction of these flows was carried out by Iacovides et al.,[1] who used a two-layer eddy viscosity model to effect numerical computations for flows, studied experimentally. The standard k-ε turbulence model was used to resolve the turbulent stresses within the main flow region, whereas the mixing-length hypothesis was used to resolve the flow in the layer immediately adjacent to the walls, instead of the usual wall functions. The authors reported that the combination of these models performed well when compared to data, in contrast to the use of a mean field closure over the whole flow coupled to wall functions, with their results demonstrating that the duct curvature induces a pair of counter-rotating vortices within its cross section. Raisee et al.[2] applied two

different low-Reynolds number, eddy viscosity-based models to study developing turbulent flows through 90°-curved ducts with square and rectangular cross sections, with both bends having an aspect ratio of 6. These authors observed that the duct curvature induced a strong secondary flow in the square duct, with the secondary motion confined to the corner regions in the rectangular cross-section case. In both cases, the secondary motion was shown to persist downstream of the bend, but to eventually disappear as the flow recovered from the influence of the bend. Quek et al.[3] presented simulations of dilute gas-solid flows in pipe bends of different radii of curvature to study particle deposition, finding that deposition takes place on entry to, and exit from, sharp bends. Mohanarangam et al.[4] used both Eulerian-Eulerian and Eulerian-Lagrangian approaches to predict gas-solid flows in a 90° bend, with comparisons of both approaches with the data of Kliafas and Holt[5] showing reasonable agreement. Their study also demonstrated that although the Eulerian-Eulerian approach gave superior agreement with data, the Eulerian-Lagrangian method was able to provide more detailed information about the particle behavior.

Kuan et al.[6,7] investigated gas-solid flow in 90° bends using a commercial computational fluid dynamics code and a Reynolds stress turbulence model. They found that their model failed to predict pressure gradient effects that prevail within the bend. Also, predicted root mean square (rms) velocity fluctuations only bore a qualitative resemblance to measured distributions, underpredicting data used in determining particle fluctuating velocities by as much as 60%.[6] In contrast, the mean streamwise gas velocities based on both the Reynolds stress and k-ε turbulence models gave a good qualitative representation of measured profiles, depending on the inlet conditions used, although Kuan et al.[7] overpredicted the mean gas velocity at the concave wall, in comparison to the data of Yang and Kuan.[8] Although these authors predicted mean fluid quantities using a Reynolds stress turbulence model, the stochastic method of Gosman and Ioannides[9] was used to model particle dispersion. The latter approach assumes isotropic, homogeneous turbulence, with the characteristic eddy velocity subsequently calculated from the kinetic energy of the turbulence. However, from earlier work flows in curved ducts are clearly anisotropic, and, hence, the stochastic method of Gosman and Ioannides[9] cannot be expected to accurately describe particle dispersion, and deposition in near-wall regions, in such flows. In addition, in investigating the physical characteristics of particle-laden flows in a square cross-sectioned 90°-duct bend, Mohanarangam et al.[4] compared an Eulerian two-fluid model and a Lagrangian particle tracking method for treating the particulate phase. These authors reported a significant underprediction of the streamwise fluctuating particle velocities, as measured by Kliafas and Holt,[5] when using the Lagrangian approach, although more satisfactory agreement was obtained with the Eulerian method.

Tian et al.[10] investigated wall roughness effects in a gas-solid flow through a 90° bend, with the gas-phase turbulence predicted using a renormalization group k-ε model. The authors achieved good agreement between numerical predictions of the mean velocity for the gas phase and the experimental data of Kliafas and Holt.[5] Sommerfeld and Huber[11] also demonstrated that wall roughness considerably affects the rebound angle of particles, which collide with walls, and, hence, the dispersion of particles within a flow.

Another phenomenon of interest in particulate flows in pipes and ducts with bends is particle roping, that is, the concentration of particles into a continuous rope, which covers a fraction of the pipe or duct cross-sectional area. The formation of such rope regions after bends causes solids concentration gradients in pneumatic conveying systems, which can create significant operational difficulties. Yilmaz and Levy[12,13] performed both physical and numerical studies on the phenomenon of rope formation after a 90° vertical bend, with their results indicating that rope formation and ultimate dispersion is strongly dependent on the radius of the bend, and less dependent on the conveying velocity and solids loading. A review of roping phenomena has been provided by Fokeer et al.[14]

The objective of the present work is to use an Eulerian-Lagrangian approach to provide accurate predictions of two-phase, gas-solid flows in a 90° bend. The numerical simulations are validated by comparisons with mean and rms velocities for both the gas and solid phases obtained in the experiments performed by Yang and Kuan.[8] To date, no previous work has demonstrated reasonable agreement with all the data available for this and similar flows when using a Lagrangian particle tracking algorithm, with fluctuating particle velocities in particular being poorly predicted. The present work, therefore, pays particular attention to the use of a turbulence model, which admits the effects of anisotropy in the gas-phase velocity fluctuations which characterize the turbulence structures which affect particle dispersion within the flow. Additionally, a random Fourier series method, which has been applied previously[15–17] to predict the instantaneous fluid velocities from the time-averaged values provided by the Eulerian fluid-phase solution has been assessed, with the overall approach capable of providing predictions of the instantaneous, anisotropic velocities experienced by particles along their trajectories. One-way coupling between the gas and particle phases was assumed given the low particle volume fraction used in the experiments utilized for validation purposes.

Eulerian Continuous Phase Model

Governing equations and numerical solution

The Eulerian approach was based on solving the partial differential equations, which describe the conservation of mass and momentum for three-dimensional, turbulent, unsteady, incompressible, isothermal flows in the absence of buoyancy through the 90° bend shown schematically in Figure 1. The mass and momentum conservation equations, expressed in time-averaged form, are given, respectively, as

$$\frac{\partial \bar{u}_i}{\partial x_i} = 0 \tag{1}$$

$$\frac{\partial \bar{u}_i}{\partial t} + \bar{u}_j \frac{\partial \bar{u}_i}{\partial x_j} = -\frac{1}{\rho}\frac{\partial \bar{P}}{\partial x_i} + \frac{\partial}{\partial x_j}\left[\nu\left(\frac{\partial \bar{u}_i}{\partial x_j} + \frac{\partial \bar{u}_j}{\partial x_i}\right) - \overline{u_i' u_j'}\right] \tag{2}$$

Here, the variables in the instantaneous forms of the transport equations have been decomposed into mean and

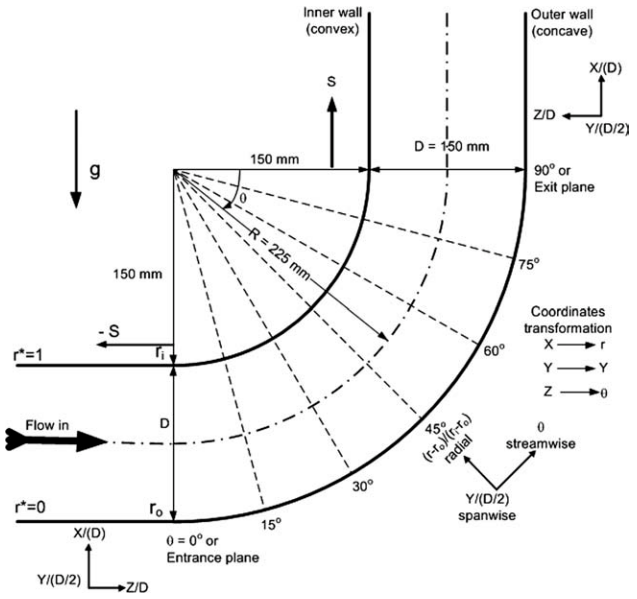

Figure 1. Schematic of the duct geometry.

fluctuating quantities, and the resulting equations time-averaged. Mean values are denoted by an overbar and fluctuating quantities by a prime. The Reynolds stress term, $\overline{u_i'u_j'}$ in Eq. 2, is unknown and must be expressed in terms of known quantities using a turbulence closure before these equations can be solved.

These equations were closed using the second-moment turbulence closure of Jones and Musonge.[18] The Reynolds stresses are obtained directly from solutions of modeled partial differential transport equations. Following,[18] the closure may be specified as

$$\frac{\partial \overline{u_i'u_j'}}{\partial t} + \bar{u}_j \frac{\partial}{\partial x_j}\left(\overline{u_i'u_j'}\right) = -\left(\overline{u_i'u_l'}\frac{\partial \bar{u}_j}{\partial x_l} + \overline{u_j'u_l'}\frac{\partial \bar{u}_i}{\partial x_l}\right) + C_s \frac{\partial}{\partial x_l}\left[\frac{k}{\varepsilon}\overline{u_l'u_m'}\frac{\partial}{\partial x_m}\left(\overline{u_i'u_j'}\right)\right] + A_{ij} - \tfrac{2}{3}\delta_{ij}\varepsilon \quad (3)$$

where k is the turbulence kinetic energy and ε its dissipation rate. The redistributive fluctuating pressure term, A_{ij}, is modeled[18,19] as

$$A_{ij} = -C_1\frac{\varepsilon}{k}\left(\overline{u_i'u_j'} - \tfrac{2}{3}k\delta_{ij}\right) + C_2\delta_{ij}\overline{u_l'u_m'}\frac{\partial \bar{u}_l}{\partial x_m} + C_3\left(\overline{u_l'u_j'}\frac{\partial \bar{u}_i}{\partial x_l} + \overline{u_l'u_i'}\frac{\partial \bar{u}_j}{\partial x_l}\right) + C_4 k\left(\frac{\partial \bar{u}_i}{\partial x_j} + \frac{\partial \bar{u}_j}{\partial x_i}\right) + C_5\overline{u_i'u_j'}\frac{\partial \bar{u}_l}{\partial x_l} - \left(\tfrac{3}{2}C_2 + C_3\right)\left(\overline{u_l'u_j'}\frac{\partial \bar{u}_l}{\partial x_i} + \overline{u_l'u_i'}\frac{\partial \bar{u}_j}{\partial x_j}\right) - \left(\frac{2}{3}C_4 + C_3\right)k\delta_{ij}\frac{\partial \bar{u}_l}{\partial x_l} \quad (4)$$

Equation 4 models A_{ij} as a general linear function of the Reynolds stress tensor under the assumption that the "return" and mean strain (or "rapid") contributions to the velocity–pressure gradient correlation, normally modeled separately, are directly influenced by mean strain. The model constants were taken as standard,[19] with $C_S = 0.22$, $C_1 = 3.0$, $C_2 = -0.44$, $C_3 = -0.46$, $C_4 = -0.23$, and $C_5 = 0.3$.

The turbulence energy dissipation rate required for solution of Eq. 3 was obtained, according to,[18–20] from

$$\frac{\partial \varepsilon}{\partial t} + \bar{u}_j\frac{\partial \varepsilon}{\partial x_j} = C_\varepsilon\frac{\partial}{\partial x_l}\left(\frac{k}{\varepsilon}\overline{u_l'u_m'}\frac{\partial \varepsilon}{\partial x_m}\right) - C_{\varepsilon 1}\frac{\varepsilon}{k}\overline{u_l'u_m'}\frac{\partial \bar{u}_l}{\partial x_m} - C_{\varepsilon 2}\frac{\varepsilon^2}{k} \quad (5)$$

where the constants in Eq. 5 were again taken as standard,[19] with $C_\varepsilon = 0.18$, $C_{\varepsilon 1} = 1.44$, and $C_{\varepsilon 2} = 1.90$.

The conservation equations were solved using an existing computer program[21] based on body-fitted co-ordinates. The main feature of the code is that it involves the transformation of independent co-ordinates to a general curvilinear co-ordinate system in a way that the physical boundaries of the flow are coincident to the transformed co-ordinate lines. This procedure allows for complex geometries to be mapped to a rectangular volume, with the computations then carried out in the transformed domain using a square finite-volume mesh. The components of velocity are not transformed, and as a consequence, are kept as dependent variables. All dependent variables, including the pressure, are stored at grid nodes and an implicit approximate factored pressure correction method is used to obtain finite-volume solutions to the flow equations. Central differencing is used for the diffusion terms, while convection terms are discretized using a bounded total variation diminishing scheme. The resulting system of quasi-linear equations is solved using preconditioned conjugate gradient methods. Overall, the method is second-order accurate in space and time. Further details can be found elsewhere.[21]

Flow domain, initial, and boundary conditions

Computations were performed for the horizontal-to-vertical flow in a square cross-sectioned duct, with a 90° bend, studied by Yang and Kuan.[8] These authors used laser Doppler anemometry to measure mean streamwise and radial velocities and associated turbulence intensities, along the direction of flow of a gas-solid mixture through a duct of side length $D = 0.15$ m, with a bend turning radius of $R/D = 1.5$. The flow rig had a horizontal straight duct section of 3.5 m length and a vertical straight duct of 1.8 m attached to the entrance and exit of the bend, respectively. Experiments were performed using an unladen air flow with a bulk velocity W_b of 10 ms^{-1}, corresponding to a Reynolds number $Re_b = 1.02 \times 10^5$, with the turbulence intensity in the main stream of the flow being approximately 1% at the center of the duct cross-section $10D$ upstream the bend.[7] The authors reported center-line flow statistics within the bend measured at seven different locations from 0° to 90°, in 15° intervals, at $3D$ and $1D$ upstream of the bend entrance in the horizontal duct section, and at $0.5D$, $1D$, $3D$, $5D$, $7D$, and $9D$ downstream of the bend exit in the vertical duct section. Further details of the initial conditions used are given in Table 1.

The complete rig was modeled in the computations performed using the co-ordinate system given in Figure 1 and a body-fitted numerical mesh. The streamwise direction is represented by the (z-θ-x) directions in the straight duct section upstream of the bend, through the bend, and in the downstream section of the duct, respectively, with the transverse or radial direction as (x-r-z) in the corresponding sections, and with the third spanwise direction corresponding to y throughout the flow domain. Nonuniform grids were used so that the distribution of grid nodes mimicked the velocity

Table 1. Initial Conditions Used in the Computations

Items	Parameters	Symbol	Units	Value min – max (mean)
Geometry	Duct diameter	D	m	0.15
	Bend radius	R	m	0.225
	Entrance length	–	m	3.5
	Exit length	–	m	1.8
	Bend radius ratio	R_r	–	1.5
Gas phase	Density	ρ	kg m^{-3}	1.18
	Viscosity	μ	kg m^{-1} s^{-1}	1.8×10^{-5}
	Bulk velocity	W_b	ms^{-1}	10
	Time step	Δt	s	1.0×10^{-5}
	Reynolds number	Re	–	1.0×10^{5}
	Turbulence intensity	I	–	1.0% of W_b
Solid phase	Mass flow rate	–	kg hr^{-1}	2
	Mass loading	L	kg kg^{-1}	2.05×10^{-3}
	Volumetric fraction	α_p	–	9.7×10^{-7}
	Density	ρ_p	kg m^{-3}	2500
	Diameter	d_p	μm	4 – 160 (77)
	Reynolds number	Re_p	–	3.17×10^{-4} – 11.5 (1.82)
	Stokes number	St	–	8.23×10^{-4} – 13.2 (3.05)
	Interparticle spacing	S/d_p	–	80.9

gradients in the duct. The computational grid for every cross-sectional plane was generated using an algebraic grid generation function, with grid lines concentrated near the walls using a hyperbolic tangent stretching function. A symmetry boundary was used to reduce the size of the computational domain rather than simulating the whole duct flow, with the vertical plane dissecting the duct constituting such a boundary, which was modeled by reflecting the values of variables on one side of this plane on to the other, with zero flow across the plane. To accurately resolve the flow in the duct along the direction of flow, streamwise nodes were clustered in the vicinity of the bend inlet and outlet using a linear tangent stretching function. Hence, in the streamwise direction, the grid contracted from the inlet toward the bend, with a uniform grid maintained within the bend itself, followed by an expanding mesh from the bend exit to the duct outflow plane. In the transverse direction, the grid contracted from the bend center-line toward the walls, allowing better resolution in close proximity to the solid surfaces.

The boundary conditions for the momentum equations were nonslip at the walls of the duct, with finite-volume solutions patched onto fully turbulent, local equilibrium wall law profiles with the matching point chosen to be at a fixed distance from the wall. As noted above, a zero-gradient symmetry boundary was used along the x-z plane through the center of the duct to reduce the size of the problem. In line with the experimental conditions, velocity components and turbulence quantities at the inlet boundary used uniform profiles determined using a representative mixing length and relative turbulence intensity as follows

$$\begin{aligned}
&\text{Mean velocities} : \bar{w} = W_b,\ \bar{u} = \bar{v} = 0\\
&\text{Turbulence kinetic energy} : k = \frac{3}{2}(W_b I)^2\\
&\text{Dissipation rate} : \varepsilon = C_\mu^{3/4} k^{3/2}/l\\
&\text{Normal stresses} : \overline{u_i' u_j'}|_{\,i=j} = \frac{2}{3}k\\
&\text{Shear stresses} : \overline{u_i' u_j'}|_{\,i\neq j} = 0
\end{aligned} \tag{6}$$

Here, I is the relative turbulence intensity, taken as 1% of the bulk velocity,[8] and l is the mixing length, which was set to $0.1D$, where D is a characteristic inlet dimension (i.e., the inlet hydraulic diameter of the duct).

Lagrangian Dispersed Phase Model

Governing equations and numerical solution

The trajectories and velocities of solid particles were simulated using the Lagrangian particle tracking approach under the assumption of one-way coupling between the gas and particle phases given that the particle volume fraction in the experiments simulated was less than 10^{-6}. After each time step, the new particle position and translational velocities were obtained from the particle equation of motion

$$\frac{d\vec{x}_p}{dt} = \vec{u}_p \tag{7}$$

$$m_p \frac{d\vec{u}_p}{dt} = \vec{F}_D + \vec{F}_g + \vec{F}_B + \vec{F}_{Sl} \tag{8}$$

where $\vec{x}_p$ and $\vec{u}_p$ are, respectively, the particle position and velocity vectors, and m_p is the particle mass. For rigid, heavy, spherical, and inert solids in a dilute gas-solid flow with a high-ratio of particle to fluid densities ($\rho_p/\rho > 10^3$), the forces considered were drag, $\vec{F}_D$, gravity, $\vec{F}_g$, buoyancy, $\vec{F}_B$, and shear lift $\vec{F}_{Sl}$. For the geometry of interest, it is also necessary to consider particle-wall collisions. Other contributions to the equation of motion from added mass, particle rotation, particle–particle collision and turbulence modulation were assumed negligible.

The drag force was computed as[7,17,22]

$$\vec{F}_D = C_D \frac{\pi}{8} d_p^2 \rho (\vec{u} - \vec{u}_p)\left|\vec{u} - \vec{u}_p\right| \tag{9}$$

with the drag coefficient, C_D, for a spherical particle with a diameter greater than one micron given as a function of the particle Reynolds number, Re_p, and drag factor, f_D, by

$$C_D = \frac{24}{\mathrm{Re}_p} f_D \quad \text{and} \quad \mathrm{Re}_p = \frac{\rho d_p |\vec{u} - \vec{u}_p|}{\mu} \tag{10}$$

Among the many expressions for f_D available in the literature, the following were the most common[22] and were used in the present simulations

$$\begin{aligned}
f_D &= 1 && \mathrm{Re}_p \le 0.2 \\
f_D &= \left(1 + 0.1\mathrm{Re}_p^{0.99}\right) && 0.2 < \mathrm{Re}_p \le 2 \\
f_D &= \left(1 + 0.11\mathrm{Re}_p^{0.81}\right) && 2 < \mathrm{Re}_p \le 21 \\
f_D &= \left(1 + 0.189\mathrm{Re}_p^{0.632}\right) && 21 < \mathrm{Re}_p \le 200 \\
f_D &= \left(1 + 0.15\mathrm{Re}_p^{0.687}\right) && 200 < \mathrm{Re}_p \le 1000 \\
f_D &= 0.44\mathrm{Re}_p/24 && 1000 < \mathrm{Re}_p \le 2 \times 10^5 \\
f_D &= 0.1\mathrm{Re}_p/24 && \mathrm{Re}_p > 2 \times 10^5
\end{aligned} \tag{11}$$

The gravity and buoyancy forces were combined[17] to give

$$\vec{F}_g + \vec{F}_B = m_p \left(1 - \frac{\rho}{\rho_p}\right) \vec{g} \tag{12}$$

where the mass of the spherical particle, $m_p = 1/6\ \pi\ d_p^3 \rho_p$, and d, ρ and μ are, respectively, the diameter, density, and dynamic viscosity, with the subscript p representing the particle, and $\vec{g}$ is the gravitational acceleration vector at the position of the particle.

The slip-shear lift force implemented was the Saffman lift, with the shear lift coefficient, C_{Sl}, included to account[7] for the high-Reynolds number according to

$$\vec{F}_{Sl} = 1.615 d_p \mu \mathrm{Re}_{Sl}^{0.5} C_{Sl} [(\vec{u} - \vec{u}_p) \times \vec{\omega}_f] \tag{13}$$

where $\vec{\omega}_f = 0.5\nabla \times \vec{u}$ is the fluid rotation, $\mathrm{Re}_{Sl} = \rho d_p^2 |\vec{\omega}_f|/\mu$ is the Reynolds number of the shear flow and C_{Sl} is the ratio of the extended lift force to the Saffman force taken[7] as

$$C_{Sl} = \begin{cases} \left(1 - 0.3314\beta^{0.5}\right) \exp(-0.1 \times \mathrm{Re}_p) & \\ \quad +0.3314\beta^{0.5} & \mathrm{Re}_p \le 40 \\ 0.0524\left(\beta \mathrm{Re}_p\right)^{0.5} & \mathrm{Re}_p > 40 \end{cases} \tag{14}$$

where $\beta = \mathrm{Re}_{Sl}/0.5\ \mathrm{Re}_p$, as proposed elsewhere.[23]

A semianalytical approach[22,24,25] was adopted for solving the equations of particle motion. The time interval during, which a particle travels is divided into subintervals, with the particle position and velocity calculated at the end of each subinterval. It is assumed that, during each subinterval, the values of the shear lift and drag factor do not change. For this assumption to be valid, the subintervals in time must be chosen to be sufficiently small, for example, 50% of the shortest of any relevant time scale such as the particle relaxation time or the integral time scale of turbulence. With the forces noted taken as constant during each subinterval, the differential equations for particle motion can be simplified using dimensional analysis, with Eqs. (7) and (8), coupled with Eqs. 9–14, solved semianalytically to obtain the particle position vector and the particle velocity in three dimensions[22]

$$\vec{x}_p = \vec{x}_p^0 + 0.5(\vec{u}_p + \vec{u}_p^0)\Delta t \tag{15}$$

$$\begin{aligned}
u_p = u - (u - u_p^{(0)}) \exp\left(-\frac{\Delta t}{\tau_p}\right) + \frac{3}{4}\frac{\rho}{\rho_p}\tau_p \left[1 - \exp\left(-\frac{\Delta t}{\tau_p}\right)\right] \\
\times \left\{ \frac{F_{Sl,x}}{m_p} - g\left(1 - \frac{\rho_p}{\rho}\right) + (w_p - w)\left[\omega_{p,y} - \frac{1}{2}\left(\frac{\partial u}{\partial z} - \frac{\partial w}{\partial x}\right)\right] \right. \\
\left. - (v_p - v)\left[\omega_{p,z} - \frac{1}{2}\left(\frac{\partial v_p}{\partial x} - \frac{\partial u_p}{\partial y}\right)\right] \right.
\end{aligned} \tag{16}$$

$$\begin{aligned}
v_p = v - (v - v_p^{(0)}) \exp\left(\frac{-\Delta t}{\tau_p}\right) + \frac{3}{4}\frac{\rho}{\rho_p}\tau_p \left[1 - \exp\left(-\frac{\Delta t}{\tau_p}\right)\right] \\
\times \left\{ \frac{F_{Sl,y}}{m_p} + (u_p - u)\left[\omega_{p,z} - \frac{1}{2}\left(\frac{\partial v}{\partial x} - \frac{\partial u}{\partial y}\right)\right] \right. \\
\left. - (w_p - w)\left[\omega_{p,x} - \frac{1}{2}\left(\frac{\partial w_p}{\partial y} - \frac{\partial v_p}{\partial z}\right)\right] \right\}
\end{aligned} \tag{17}$$

$$\begin{aligned}
w_p = w - (w - w_p^{(0)}) \exp\left(-\frac{\Delta t}{\tau_p}\right) + \frac{3}{4}\frac{\rho}{\rho_p}\tau_p \left[1 - \exp\left(-\frac{\Delta t}{\tau_p}\right)\right] \\
\times \left\{ \frac{F_{Sl,z}}{m_p} + (v_p - v)\left[\omega_{p,x} - \frac{1}{2}\left(\frac{\partial w}{\partial y} - \frac{\partial v}{\partial z}\right)\right] \right. \\
\left. - (u_p - u)\left[\omega_{p,y} - \frac{1}{2}\left(\frac{\partial u_p}{\partial z} - \frac{\partial w_p}{\partial x}\right)\right] \right.
\end{aligned} \tag{18}$$

$$\tau_p = \frac{\rho_p d_p^2}{18 \mu f_D} \tag{19}$$

where τ_p is the response (relaxation) time of a particle to changes in the flow field. The u_p, v_p and w_p values used in this equation set represent the particle velocity components in the x, y, and z directions, respectively. Gravitational acceleration, g, acts only in the (negative) vertical direction, and, hence, only appears in Eq. 16 for u_p. In all the sections of the duct considered, the x axis and the u_p velocity are, therefore, aligned with the vertical direction, which is the opposite sense to gravity. These velocities (u_p, v_p, and w_p) are computed at every instant and subsequently resolved into the streamwise, transverse, and spanwise directions, as shown in Figure 1. In doing so, the gravitational force is accounted for in computations in all sections of the duct.

During solution, each particle size considered is tagged and assigned an initial position. The particle's path is then tracked by continually updating its spatial position with time, using particle velocities computed from the sum of the mean fluid velocities obtained from the Eulerian solution, and the velocity fluctuations obtained from the random Fourier series method described below. The particle tracking algorithm is then used to obtain solutions to Eqs. 16–18 for each individual particle.

As noted, in solving for the particle motion, it is necessary to choose an integration time step smaller than the particle relaxation time, as well as being sufficiently small to capture the moment when a particle traverses a computational cell or a turbulent eddy.[26] If the particle moves slowly relative to the fluid, it will remain in the eddy during the whole lifetime of that eddy, τ_e. However, if the relative velocity between

the particle and the fluid is appreciable, the particle will traverse the eddy in its transit time, τ_r. Thus, the integral time step is given as[9,26]

$$\Delta t = 0.5 \times \min\left(\tau_p, \tau_e, \tau_r, \ \tau_{cv}\right) \tag{20}$$

where τ_p denotes the particle relaxation time defined in Eq. 19, and the lifetime of the eddy, τ_e, is given by

$$\tau_e = l_e\left(\frac{2}{3}k\right)^{1/2} \ \text{with} \ \ l_e = \left(C_\mu k^2\right)^{3/4}/\varepsilon \tag{21}$$

where l_e is the eddy length scale. The time required by a particle to transverse an eddy, that is, its transit time, τ_r, is given by

$$\tau_r = -\tau_p \ln\left(1 - \frac{l_e}{\tau_p|\vec{u} - \vec{u}_p|}\right) \tag{22}$$

with τ_{cv} representing the time taken by a particle to cross the entire control volume, given by

$$\tau_{cv} = \min\left(\frac{\Delta x}{u_p}, \frac{\Delta y}{v_p}, \frac{\Delta z}{w_p}\right) \tag{23}$$

After each interaction between the particle and a turbulent eddy, a new fluctuating velocity is assumed as the particle continues to traverse the flow field. It should be noted that the values of k and ε are assumed constant for the duration of the lifetime of the eddy.

Particle dispersion model

The instantaneous fluid velocity, $\vec{u}$, required in the force terms was computed from the summation of time-averaged fluid velocities, obtained from the Eulerian solution, and fluctuating velocities

$$\vec{u} = \vec{\bar{u}} + \vec{u}' \tag{24}$$

The fluctuating velocities were determined using a random Fourier series[15–17] approach as

$$\begin{aligned} u' &= \sum_{i=1}^{N} \gamma_1 U_{m,i} \cos(\omega_i \ \Delta t - \gamma_2 \ \alpha_{u,i}) \\ v' &= \sum_{i=1}^{N} \gamma_3 V_{m,i} \cos(\omega_i \ \Delta t - \gamma_4 \ \alpha_{v,i}) \\ w' &= \sum_{i=1}^{N} \gamma_5 W_{m,i} \cos(\omega_i \ \Delta t - \gamma_6 \ \alpha_{w,i}) \end{aligned} \tag{25}$$

where γ_1 to γ_6 are random numbers sampled from a uniform probability distribution between zero and unity. The frequency, ω_i, is obtained from a Gaussian distribution with a standard deviation of unity. $\alpha_{u,i}$, $\alpha_{v,i}$ and $\alpha_{w,i}$ are the initial fluctuating phases of the u, v, and w fluctuating velocities, which are randomly sampled between 0 and 2π. N (=100) is the number of terms considered in the series. $U_{m,i}$, $V_{m,i}$ and $W_{m,i}$ are the amplitudes of fluctuation obtained as a function of the fluid Reynolds normal stresses, and the turbulence energy spectrum, E_i, according to

$$\begin{aligned} U_{m,i}^2 &= E_i\overline{u'u'} \\ V_{m,i}^2 &= E_i\overline{v'v'} \\ W_{m,i}^2 &= E_i\overline{w'w'} \end{aligned} \tag{26}$$

where E_i is the energy distribution ratio with respect to the frequency ω_i given by

$$E_i = \frac{\int_{\omega_i}^{\omega_{i+1}} E(\omega)d\omega}{\int_0^{\infty} E(\omega)d\omega} \tag{27}$$

The turbulent energy spectrum $E(\omega)$ used was that measured by Laurence,[27] and as used and applied by Fan et al.[15]

$$E(\omega) = 16\left(\frac{2}{\pi}\right)^{1/2}\omega^4 \exp(-2\omega^2) \tag{28}$$

where ω is the wave number.

Initial and boundary conditions

The Lagrangian approach can track only a moderate number of particles because of the computational cost and time required to compute their trajectory. Because of this, the tracking algorithm is assumed to represent parcels of particles, where each parcel represents a large bulk of particles with the same size, density, velocity, and position. In the experiment considered further below,[8] the particles used were polydispersed and, accordingly, the appropriate size distribution was included in the model. The Eulerian flow solutions for half of the duct geometry were first mapped onto the full cross-sectional area of the duct before applying the random Fourier series model and the Lagrangian particle tracking. Particles were introduced into the computational domain in parcels over 400 initial locations, which were randomly distributed across the inlet plane of the duct. In the simulations, up to 1.0 million particle trajectories were computed, with results derived using one million particles found to give particle statistics, which were independent of the number of particles used. Further details of the initial conditions used are given in Table 1.

In contrast to the Eulerian approach for the carrier phase, where equations for averaged flow quantities are solved, in the Lagrangian approach for the dispersed phase, the particle velocities must be sampled and subsequently averaged. Mean and rms values of particle characteristic velocities, φ_p, were evaluated in each computational cell according to[7]

$$\bar{\varphi}_p = \frac{\sum_{i=1,12}\varphi_p n_i \xi_i}{\sum_{i=1,12} n_i \xi_i} \tag{29}$$

where n_i is the number of particle tracks for size fraction i, and ξ_p is the corresponding particle number flow rate per particle track. The particles were grouped into 12 particle-size fractions.[7] The fluctuation about the mean is defined as $\varphi'_p = \varphi'_p - \bar{\varphi}_p$, such that the root mean square of the turbulent fluctuation in φ is given by

$$\sqrt{\overline{(\varphi'_p)^2}} = \left(\frac{1}{N}\sum_{i=1}^{N}(\varphi'_p)^2\right)^{1/2} \tag{30}$$

where N is the total number of particles of all sizes.

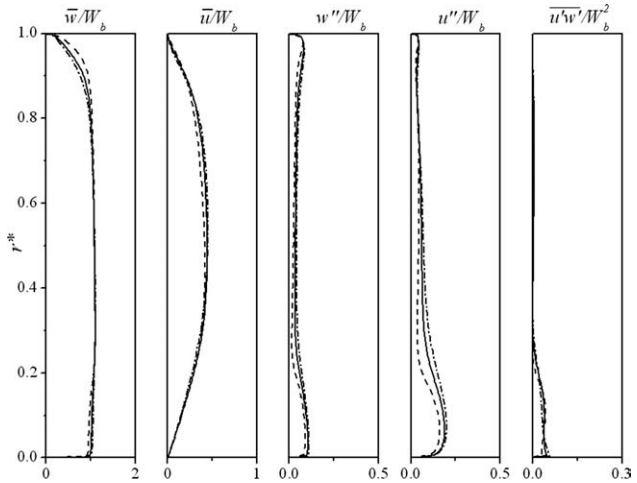

Figure 2. Predictions of mean gas velocities, and normal and shear stresses, at the exit of the duct bend (—— 640 k, — 1,440 k, and –·– 2,560 k nodes).

The Lagrangian approach also requires the tracking of the particles' trajectories before and after collisions with a boundary wall. This work considers rough rigid walls; hence, the hard-sphere model, which implies negligible particle deformation during the impact process was applied. A particle collides with a boundary when its center is one radius from the wall, and it loses a fraction of its momentum before being reintroduced back into the bulk flow. The change in particle momentum due to impact is a function of the particle impact velocity $\vec{u}_p^{(1)}$, the properties of the wall material, and the particle incidence angle θ_1. The influence of wall collisions was consequently modeled with the aid of experimental measurements of particle restitution coefficients[28] in the form of least square fits to polynomial functions as

$$e_n = \frac{u_{p,n}^{(2)}}{u_{p,n}^{(1)}} = 0.993 - 1.76\theta_1' + 1.56\theta_1'^2 - 0.49\theta_1'^3 \tag{31}$$

$$e_t = \frac{u_{p,t}^{(2)}}{u_{p,t}^{(1)}} = 0.988 - 1.66\theta_1' + 2.11\theta_1'^2 - 0.67\theta_1'^3 \tag{32}$$

where $u_{p,n}$ and $u_{p,t}$ represent the particle velocity impact components normal and tangential to the wall, and superscripts (1) and (2) refer to the conditions before and after impact, respectively.

To simulate the effect of wall roughness on particle-wall interactions, a stochastic approach based on the work of Sommerfeld[11] and Huber[25] was adopted. The impact angle θ_1' was assumed to be composed of the particle trajectory angle θ_1 from a smooth wall and a stochastic contribution due to wall roughness

$$\theta_1' = \theta_1 + \Delta\gamma\xi \tag{33}$$

where $\Delta\gamma\xi$ represents a random component sampled from a Gaussian distribution function, with ξ a Gaussian random number with zero mean and standard deviation of unity. Note that the units of theta (symbol) in Eq. 33 are degrees, whilst elsewhere theta (symbol) is in radians. From experiments[11] and numerical simulations,[10,11,25] it has been found that the probability of the wall roughness angle may be approximated by a normal distribution function with a standard deviation of $\Delta\gamma$. The value of $\Delta\gamma$ depends on the structure of the wall roughness and on the particle size. In this study, a wall roughness angle $\Delta\gamma$ of 3.8° was used,[11] as this value corresponds to 100 μm glass particles impacting on a Plexiglass surface, which is similar to the materials used in the experiments.[8]

Results and Discussion

Fluid phase

Grid independence of the numerical solutions for the fluid phase was examined using a number of meshes, with results at the exit of the bend derived using grids of 640 k, 1,440 k and 2,560 k nodes given in Figure 2. This location is particularly sensitive to the grid resolution used due to the influence of streamline curvature and pressure gradients caused by flow through the bend. Note that, in this figure, double prime is used to represent the rms of a fluctuating velocity. Predictions obtained using the latter two meshes, consisting of 120 × 60 × 200 and 160 × 80 × 200 nodes in the transverse, spanwise, and streamwise directions, respectively, show few differences, with the larger grid providing results, which were effectively independent of grid resolution with acceptable computational costs.

Figure 3 shows the streamwise distribution of the pressure coefficient across the transverse (radial) direction for the entire length of the curved duct. The pressure coefficient C_p is defined[2,29] by

$$C_p = \frac{P - P_{in}}{0.5 \times \rho W_b^2} \tag{34}$$

where P_{in} is the gas pressure at the inlet and W_b the bulk mean velocity of the gas. The dimensionless radial position, r*, according to the configuration in Figure 1 is defined by

$$r* = \frac{r - r_o}{r_i - r_o} \tag{35}$$

where r_o and r_i are the outer and inner duct radii, respectively. Figure 3 shows the pressure coefficient at difference locations

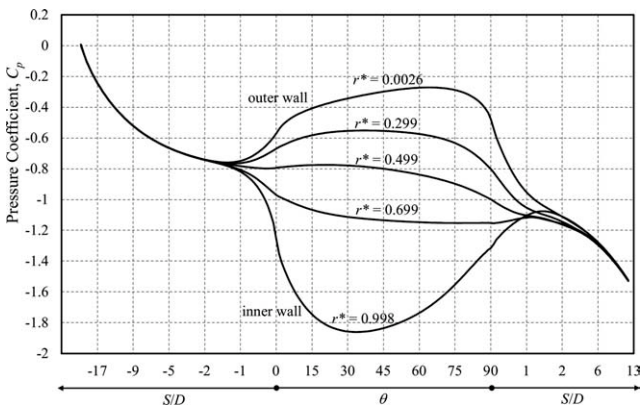

Figure 3. Pressure coefficient distribution at different radial locations along the duct length.

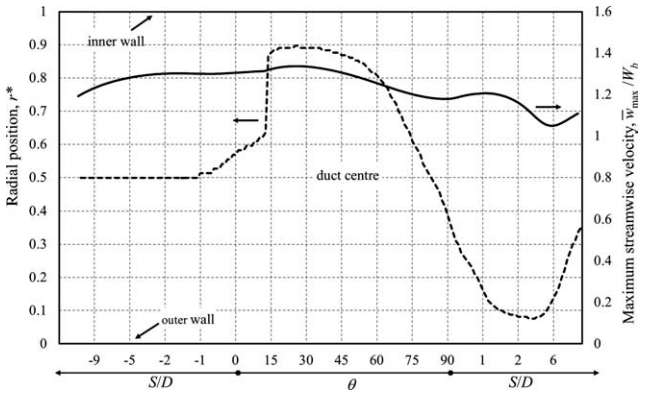

Figure 4. Gas-phase peak streamwise mean velocity and its radial location along the duct length (..... r*, — $\overline{w}_{max}/W_b$).

within the duct. The closest grid lines to the duct walls are at $r^* = 0.003$ and $r^* = 0.998$, close to the outer and inner walls, respectively. Other positions considered are at the center, $r^* = 0.5$, of the duct, and at $r^* = 0.3$ and 0.7. The distribution of the pressure coefficient throughout the duct gives insight into the behavior of the fluid. From the results of Figure 3, there is clearly a large pressure gradient around the duct bend, with constant pressure away from the bend in both the upstream and downstream directions. From the fluid inlet location at $S/D = -23$ up to $S/D = -2$, the pressure coefficient is uniform across the duct. A slight difference in the pressure coefficient starts from around $S/D = -2$ and continues up until the middle of the bend where the pressure gradient is a maximum. This difference continues until the 90° plane at which point it starts to diminish downstream of the bend, although the influence of the bend continues to affect the fluid up to $S/D = 12$. This observation that the bend influences fluid flow from upstream locations of $S/D \approx -2$ to downstream distances of $S/D \approx 12$ has been noted previously in both experimental[27] and numerical[30,31] studies.

Figure 4 shows the distribution of the peak streamwise mean velocity across the duct, and the radial position, r^*, where the peak value occurs. Figure 5 also gives streamwise mean velocity vectors for the fluid phase on the plane of symmetry ($y/D = 0.5$) and at several locations along the duct. Upstream of the bend ($S/D < -2$), the fluid flow is symmetric with the maximum mean velocity at the center of the duct. At these locations, the flow is yet to be influenced by the bend, as also revealed in the pressure coefficient results of Figure 3, which show an approximately constant value across the duct in these regions. As the flow advances closer to the bend, as shown from $S/D > -1$, the fluid velocity becomes slightly skewed, with a slight acceleration near the inner wall and a slight deceleration near the outer wall of the duct; this induces a cross-stream movement of the peak velocity toward the inner wall of the bend. This phenomena is further confirmed by the commencement of a significant pressure gradient across the duct, as shown in the pressure coefficient results from $S/D = -1$ in Figure 3. The shift in the peak streamwise means velocity toward the inner bend radius from this location is, as a result of the centrifugal effect and a weak inward cross-stream flow, induced in the cross-section of the bend. This leads to acceleration of the fluid near the inner convex wall due to the favorable streamwise pressure gradient, and a deceleration of the fluid near the concave wall because of the developed adverse pressure gradient, between $\theta = 0°$ and 30°. It has also been shown that this streamwise velocity gradient increases with increasing bend turning angle.[29] The maximum mainstream velocity occurs at $\theta = 26°$ (Figure 4) with a value of $1.34W_b$ and at a radial position $r^* = 0.90$ on the symmetry plane. The developed velocity gradient then persists with downstream distance, with a reversal of the location of the peak velocity toward the outer wall, leading to a deceleration near the convex wall and an acceleration near the concave wall between $\theta = 30°$ and 90°. The effect of the bend on the flow continues downstream of the bend, with the peak velocity remaining close to the outer wall of the duct. Only at distances of the order of $S/D > 12$ beyond the bend does the flow return to normality and re-establish a symmetric velocity profile with a peak at the center of the duct.

Figures 6 and 7 compare the experimental and predicted streamwise mean gas velocities along the symmetry plane of the duct, normalized by the bulk velocity, at $\theta = 0°$ to 90° in intervals of 15° within the bend section (Figure 6), and both upstream, $S/D = -3.0$ and -1.0, and downstream, $S/D = 0.5$, 1.0, 3.0, 5.0, 7.0, and 9.0, of the bend (Figure 7). In general, the numerical simulation successfully predicts the behavior of the flow in the central regions of the duct, and close to the outer walls. Upstream of the bend, the peak mean velocity occurs at the duct center ($r^* = 0.5$), whereas at the entrance to the bend section ($\theta = 0°$), the peak occurs at a radial position corresponding to $r^* = 0.57$. Once within the bend, the location of the peak velocity becomes further skewed toward the inner convex wall, with the peak at the middle of the bend ($\theta = 45°$) occurring at a radial position of $r^* = 0.87$. In Figure 6, there is a slight overprediction of the streamwise mean velocity in the boundary layer close to the concave wall between $\theta = 30°$ and 60°, which may be a

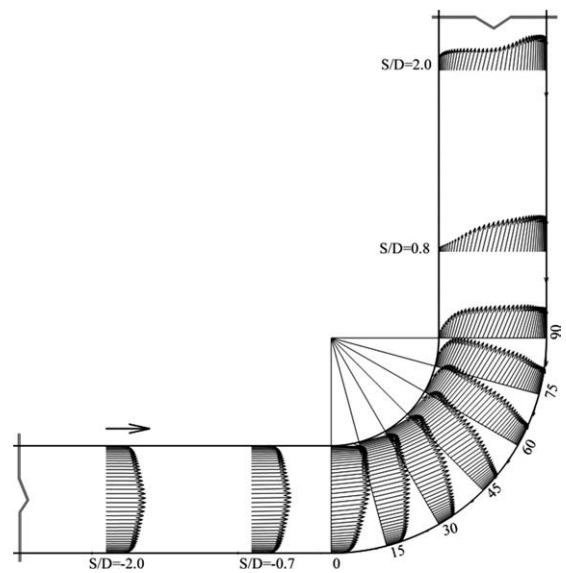

Figure 5. Gas-phase streamwise mean velocity vectors at selected planes along the duct length.

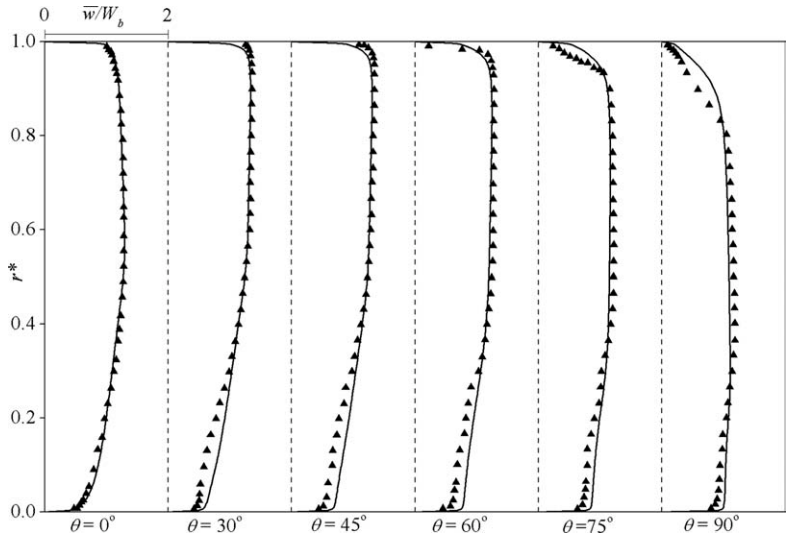

Figure 6. Comparison between predicted and measured gas-phase streamwise mean velocities in the duct bend (▲ measured, — predicted).

result of the adverse pressure gradient that exists in this region of the bend, as shown in Figure 3. There is also slight underprediction of the mean velocities near the convex wall at $\theta = 45°$, and to some extent at $\theta = 60°$, which becomes a significant overprediction at $\theta = 75°$ and 90°. This overprediction persists beyond the bend and away from the upper wall at $S/D = 0.5$, as shown in Figure 7, although by $S/D = 1.0$ predicted velocities are qualitatively incorrect in the upper half of the duct, both underpredicting data close to the upper wall, and overpredicting data toward the duct center. By $S/D = 3.0$, however, predictions are again in line with experiment. These regions of the flow are particularly difficult to predict coinciding, as they do, with the abrupt reversal of the main stream flow, with the peak velocity moving from locations close to the convex wall in the first half of the bend toward the concave wall in the second half, and continuing downstream of the bend. This reversal in the flow drives the peak velocity at the exit of the bend to around $r^* = 0.39$, and just downstream the bend, at $S/D = 0.5$, the peak continues to migrate toward the outer wall under the influence of centrifugal forces, occurring at $r^* = 0.22$ at this location. Further downstream the effect of the bend reduces and the flow gradually adjusts to symmetrical behavior, as the peak velocity moves away from the outer wall back to the center of the flow. Overall, the model captures the main features of the flow within the duct and the bend section, in agreement with experimental findings,[8] although there are shortcomings as noted above.

Figures 8 and 9 compare the available experimental data and predicted transverse (radial) mean gas velocities within the bend and in the vertical section of the duct beyond the bend. There is good agreement between the data and predictions, with the figures showing a positive transverse velocity occurring at the entrance to the bend ($\theta = 0°$), whereas negative transverse velocities occur everywhere else, both in the bend and the vertical duct section. These negative radial

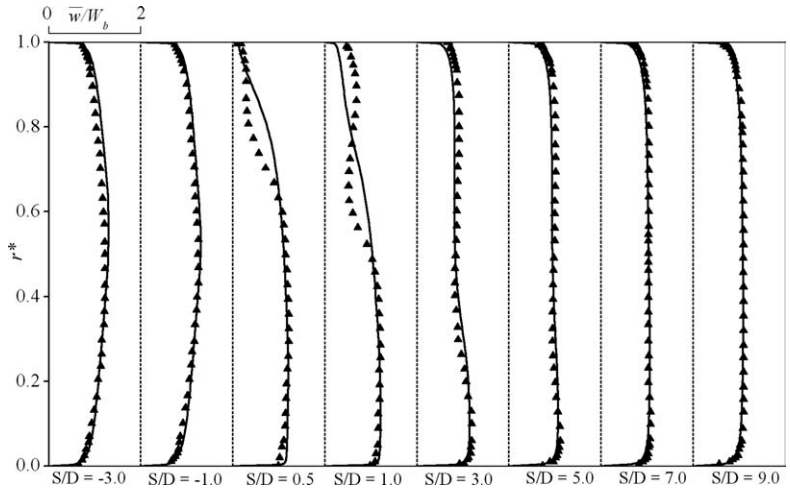

Figure 7. Comparison between predicted and measured gas-phase streamwise mean velocities upstream and downstream of the duct bend (▲ measured, — predicted).

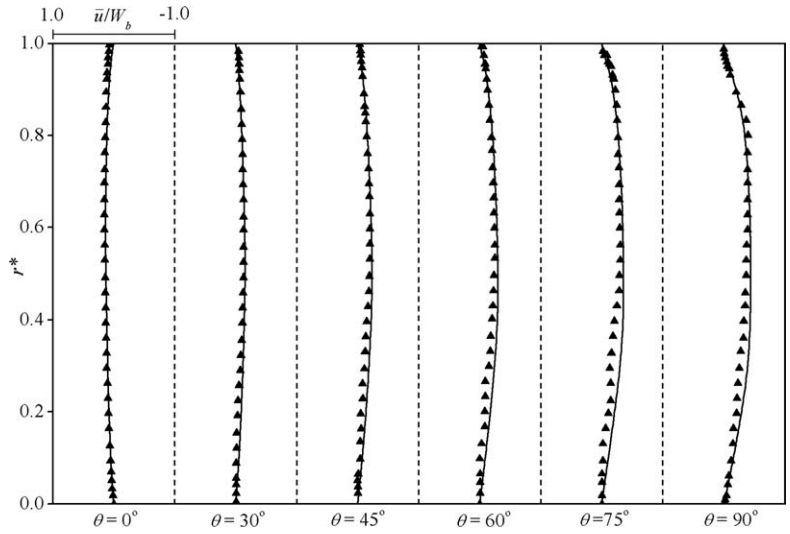

Figure 8. Comparison between predicted and measured gas-phase radial mean velocities in the duct bend (▲ measured, — predicted).

velocities may be attributed to the redirection of the flow and the movement of the peak streamwise mean velocity from locations close to the inner radius of the bend toward its outer radius. The magnitude of the negative velocities also increases with distance through the bend and beyond, only starting to recover from $S/D = 3.0$. Overall, the predictions are in line with experiment, particularly in the bend section, although these is an overprediction of the traverse velocity in the upper half of the duct at $S/D = 0.5$ and 1.0, coinciding with the inaccuracies noted in prediction of the streamwise mean velocity.

Predictions of the streamwise rms fluctuating velocity are compared with experimental data in Figure 10 for the bend section, and in Figure 11 for the straight sections of the duct. There is clearly a slight underprediction of the magnitude of the turbulence intensity at the outer wall in the first half of the bend, with the model also underpredicting fluctuating velocities at the inner wall in the second half of the bend. The latter underprediction also continues beyond the bend, at $S/D = 0.5$ and 1.0, although by $S/D = 3.0$ the predictions are in agreement with data. Both the predictions and data indicate that turbulence is damped near the inner convex wall in the first half of the bend, whereas turbulence enhancement occurs in the same region in the second half of the bend. Again, the model predictions are generally in line with data, apart from at those locations where shortcomings were also noted in both the mean streamwise and transverse velocities, namely close to the inner wall of the bend at $\theta = 75°$ and 90°, and just beyond the bend in the upper regions of the duct at $S/D = 0.5$ and 1.0.

Overall, the present predictions of the gas phase compare favorably with the previous results of Kuan et al.[7] who used

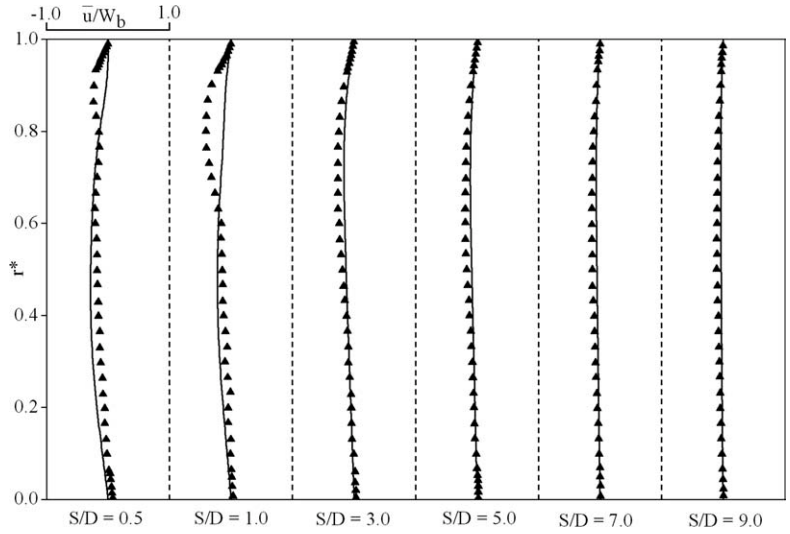

Figure 9. Comparison between predicted and measured gas-phase radial mean velocities downstream of the duct bend (▲ measured, — predicted).

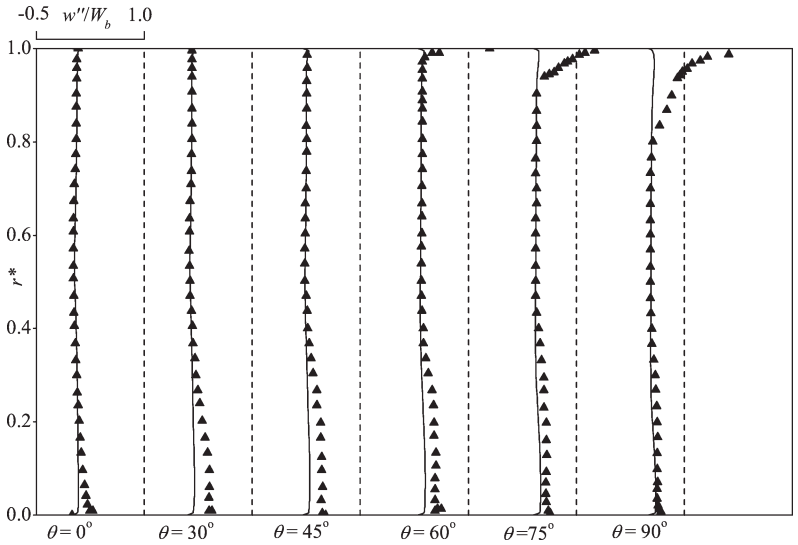

Figure 10. Comparison between predicted and measured gas-phase streamwise rms fluctuating velocities in the duct bend (▲ measured, — predicted).

a commercial CFD code embodying a differential Reynolds stress closure to predict this flow.[8] The present results for mean velocities in the streamwise and transverse directions are, therefore, in closer accord with data, with Kuan et al.[7] also predicting flow separation on the inner wall of the bend at $\theta = 90°$, which is not observed in the data of Yang and Kuan[8] or the results, herein. Similar to this work, predictions[7] of the streamwise fluctuating velocity again underpredicted data on the inner wall of the bed at $\theta = 75°$ and 90°, and at the entrance to the vertical section of the duct at $S/D = 0.5$. At these locations within the bend, the flow on the inner wall is experiencing an adverse streamwise pressure gradient, which can modify the flow turbulence and ultimately lead to flow separation, with increases in turbulence attributable to the production of turbulence energy by the streamwise velocity gradient. However, there is little evidence in support of this in the experimental data, with no indication of flow separation. Data are only available, however, on the vertical plane dissecting the duct, and these effects may be occurring elsewhere leading to the enhanced turbulence levels observed experimentally. The mean streamwise velocity predictions of the present work also compare favorably with those of Ibrahim et al.,[32] who used standard and RNG-based k-ε turbulence models to predict these data.[8]

Particle phase

Predictions of the particle phase data given in Yang and Kuan[8] were made using the three-dimensional Lagrangian particle tracking approach described earlier. In line with the

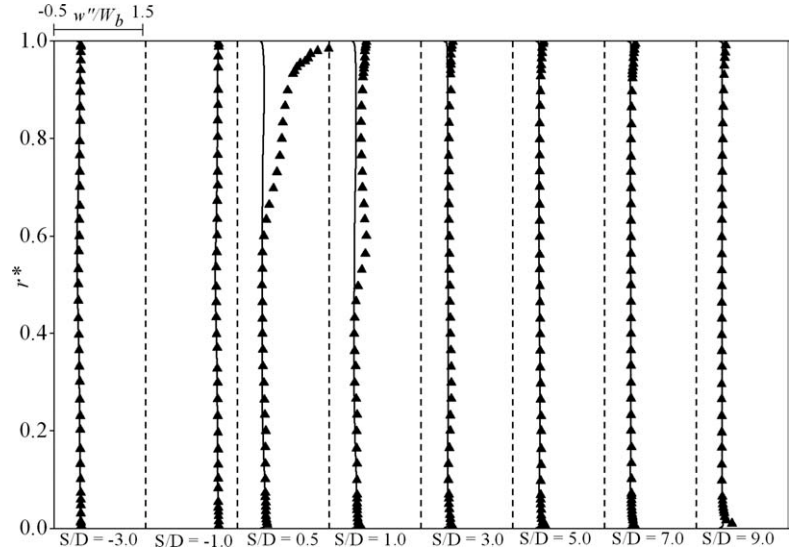

Figure 11. Comparison between predicted and measured gas-phase streamwise rms fluctuating velocities upstream and downstream of the duct bend (▲ measured, — predicted).

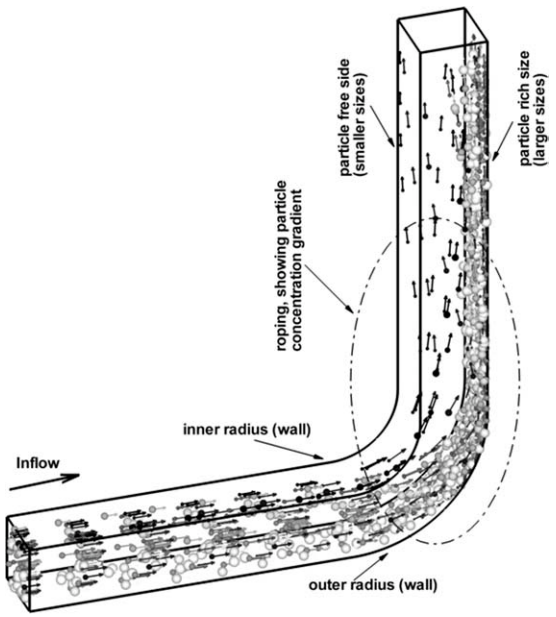

Figure 12. Polydispersed particle dispersion in the duct.

experiments performed,[8] the predictions used polydispersed particle sizes ranging from 4 to 160 μm, with a mean diameter of 77 μm. The particles were grouped into 12 different size fractions, as noted above, centered around 5, 18, 30, 45, 57, 65, 76, 89, 103, 125, 140, and 152 μm. The size fraction was determined based on the particle loading and flow rate,[8] and a fixed number of particle tracks were allocated to each size fraction.

Figure 12 shows a scatter and vector plot of the trajectories of 60 particles per size fraction at different times as the particles pass through the duct, with the particle sizes plotted as d_p/D, that is, normalized by the duct diameter. This figure serves to highlight the dispersion of particles within the duct, and the phenomena of particle roping. Although some small particles ($d_p/D \approx 3.3 \times 10^{-5}$) with low-Stokes numbers are evenly distributed across the duct cross-section, fewer particles are in general found in the region near the inner wall of the bend, with the majority of particles, with higher Stokes numbers, driven toward the outer wall of the duct due to the effects of inertia and gravity. There is also a gradient in the distribution of particle sizes across duct. The thickness of the particle free region gradually increases until the bend exit, and persists downstream into the vertical section of the duct where collisions with the wall decrease the kinetic energy of the particles and maintain the high-concentration of particles close to the outer wall. The resuspension of these particles back into the mainstream of the flow following the bend depends on the amount of momentum retained after collision with the wall. Both small and large particles within the vicinity of the boundary layer on the outer wall, therefore, collide with the wall surface and those with sufficient kinetic energy are resuspended back into the mainstream of the flow, whereas those that loose significant amounts of energy through collisions frequently roll or deposit on the wall. Particle-wall interaction is, thus, a controlling factor affecting the distribution of particles beyond the bend. These observations are in line with previous investigations, which observed a gradient in the distribution of particle sizes across the duct, with smaller particles concentrating at the inner wall region, whereas larger particles occurred closer to the outer wall.[7,12,13]

The particle mass loading of 0.00206 used in the experiments corresponds to a particle volume fraction of 9.72×10^{-7}, which means that the suspension is effectively dilute. At $\alpha_p \leq 10^{-6}$, therefore, the fluid-phase momentum can be considered independent of that of the solid phase, hence, one-way coupling between the phases has been assumed in line with the approach taken in previous studies. This holds true in

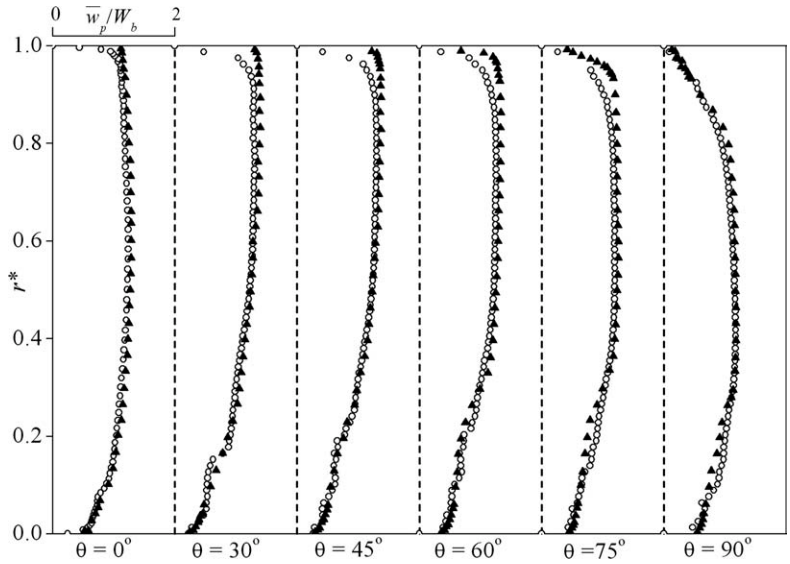

Figure 13. Comparison between predicted and measured particle streamwise mean velocities in the duct bend (▲ measured, ○ predicted).

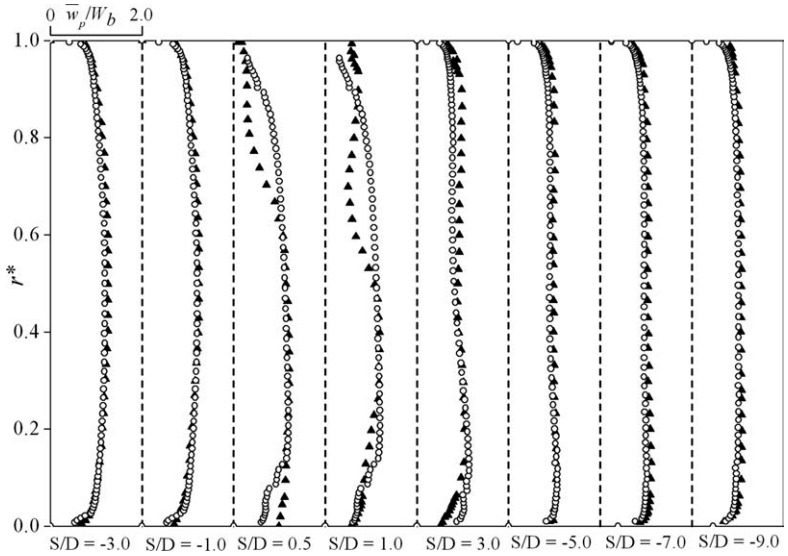

Figure 14. Comparison between predicted and measured particle streamwise mean velocities upstream and downstream of the duct bend (▲ measured, ○ predicted).

the straight duct section upstream of the bend, at the bend entrance, and through the bend to the location before the commencement of particle roping. However, as particle roping occurs close to the bend exit and progresses through to the downstream section of the duct, the accumulation of particles around the outer wall creates a significant particle concentration gradient, which may increase the particle mass loading in these regions to a level where two-way coupling might influence the fluid momentum. These effects are ignored in the present work, although are worthy of consideration in future studies. Despite this neglect, however, predictions of gas velocities in regions of the flow where particle roping occurs are seen to be in good agreement with data.

Figures 13 and 14 compare predictions of mean streamwise particle velocities within the bend and straight sections of the duct, respectively, with the experimental data of Yang and Kuan.[8] There is good agreement between the predictions and data within the bend section, and it is interesting to note that the particle-wall interaction model in general successfully predicts the change in momentum of the particles, with the resolution and transformation of the incident and rebound particle velocities in three dimensions within this section of the duct performing well. In particular, the restitution coefficient used, from experimental data,[28] appears to resolve the momentum change successfully after particles have collided with the outer wall. However, there is some underprediction of the mean streamwise particle velocity close to the inner wall of the bend, as shown in Figure 13. Mean gas velocities, given in Figure 6, were generally in line with data close to the inner duct wall at $\theta = 0^\circ$ to 60°, although data

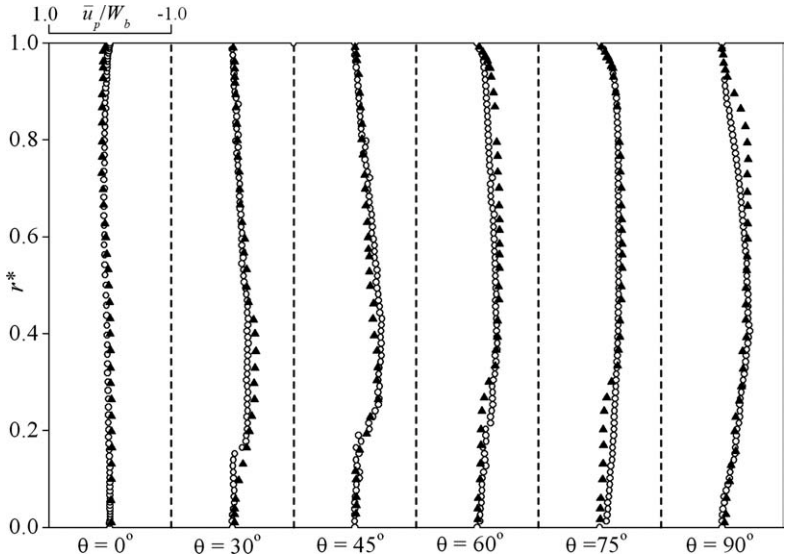

Figure 15. Comparison between predicted and measured particle radial mean velocities in the duct bend (▲ measured, ○ predicted).

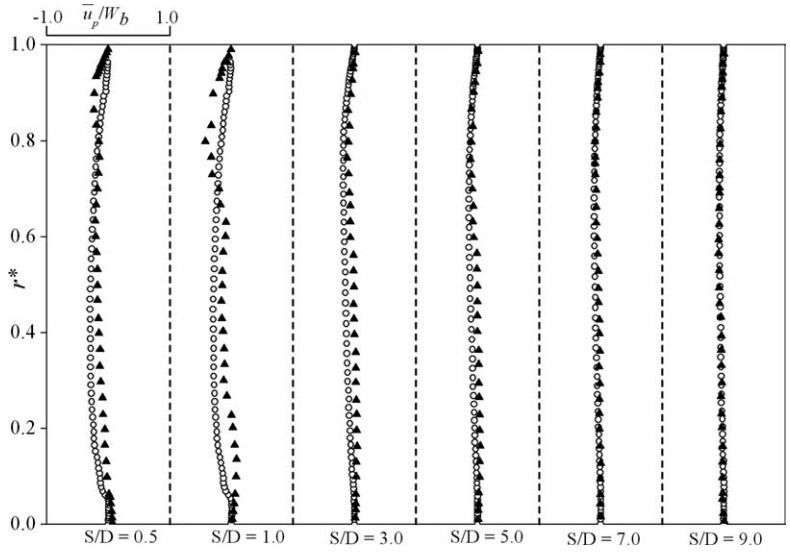

Figure 16. Comparison between predicted and measured particle radial mean velocities downstream of the duct bend (▲ measured, ○ predicted).

were slightly overpredicted at $\theta = 75°$ and 90°. In this region of the flow, there was also a preponderance of small particles and, as a consequence, they would be expected to follow the fluid streamlines, with few particle-wall interactions. Some underprediction of the particle data close to $r^* = 1$ at $\theta = 0°$ are, however, apparent in Figure 13, and this difference is then accentuated between $\theta = 30°$ and 75°, but recovers by the exit of the bend. Uncertainties in the precise inlet conditions for the particles used experimentally may be a contributory factor to the differences observed, although it is likely that the particle tracking approach failed to capture the acceleration of the gas phase in this region of the flow. Over the rest of the duct cross-section, however, good agreement with data is obtained.

In Figure 14, there is again good agreement between the predicted mean streamwise particle velocities and data upstream of the bend, that is, at $S/D = -3.0$ and -1.0, although some slight differences occur on the upper wall at both locations, which appear to be amplified by $\theta = 0°$, as noted above. There are also some obvious discrepancies in the vertical section of the duct beyond the bend exit, particularly at $S/D = 0.5$ and 1.0. These differences may, however, be attributed to shortcomings in the predicted mean gas velocity profiles in this region, as shown in Figure 7, with the smaller particles close to the inner wall clearly able to follow the mean gas flow.

Predicted mean transverse particle velocities and experimental data within the bend and straight sections of the duct

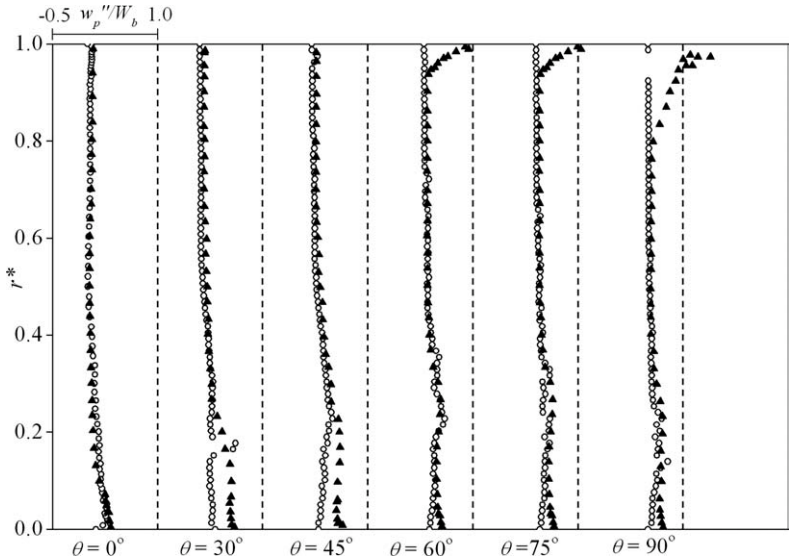

Figure 17. Comparison between predicted and measured particle streamwise rms fluctuating velocities in the duct bend (▲ measured, ○ predicted).

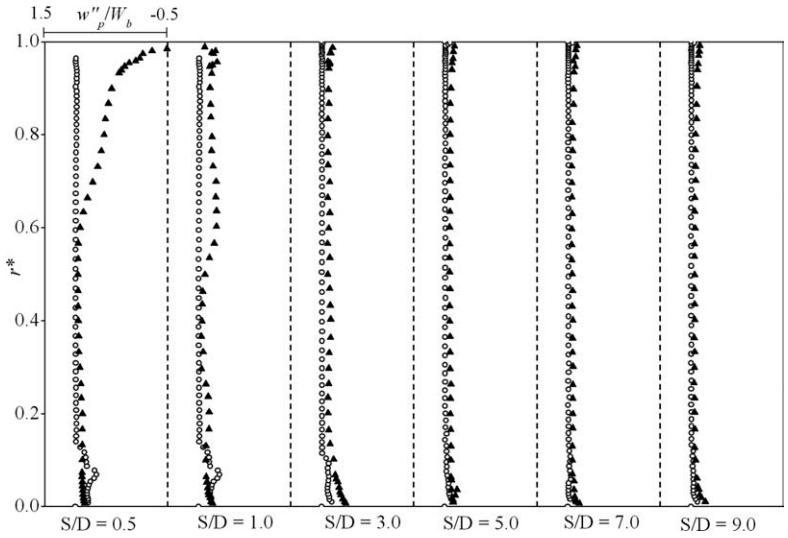

Figure 18. Comparison between predicted and measured particle streamwise rms fluctuating velocities downstream of the duct bend (▲ measured, ○ predicted).

are shown, respectively, in Figures 15 and 16. In general, the predictions reproduce the experimental data, with good agreement within and downstream of the bend regions, apart from at the exit of the bend, at $S/D = 0.5$ and 1.0, where the particles again conform with the gas velocities of Figure 9, which tend to underpredict data in the lower sections of the duct, and overpredict data close to the inner wall. This is also true of the particle streamwise fluctuating velocities given in Figures 17 and 18, with the particle velocities closely following the fluctuating gas velocities of Figures 10 and 11, which leads to an underprediction of data near the outer wall of the bend at $\theta = 30^\circ$ and 45°, and a more significant under-prediction near the inner wall at $\theta = 60^\circ$ to 90°. The latter underprediction also persists into the vertical section of the duct, at $S/D = 0.5$ in Figure 18, although as the flow recovers from the influence of the bend predictions again fall in line with data.

Results for the particle phase again compare favorably with those of Kuan et al.,[7] who also predicted this flow[8] with the present mean particle velocities in the streamwise and transverse directions in closer agreement with data. Importantly, the results, herein, also demonstrate that the anisotropic, random Fourier series approach to modeling particle dispersion yields reasonable predictions of the instantaneous fluid velocities required by the particle tracking routine. These in turn give particle fluctuating velocities in acceptable agreement with data, particularly when the shortcomings of the present gas-phase predictions are taken into account. This contrasts with earlier studies[4,6,7] that used the stochastic approach of Gosman and Ioannides[9] based on the assumption of isotropic turbulence, to model particle dispersion. Mohanarangam et al.,[4] therefore, reported that their approach, based on that of Gosman and Ioannides,[9] could not quantitatively predict particle velocity fluctuations, whereas Kuan et al.[6,7] did not report predictions of the latter fluctuations. Additionally, the mean particle velocities given in this work were based on three-dimensional Lagrangian particle tracking and particle-wall interaction algorithms, with the results presented obtained using one million particle trajectories. This contrasts to the work of Kuan et al.,[7] who used a two-dimensional particle-wall interaction model, and 96 k particles. This goes some way in explaining the differences noted in the predicted mean particle velocities between the two works.

Conclusions

A particle-laden turbulent flow in a square cross-sectioned duct with a 90° bend has been modeled using a three-dimensional Eulerian-Lagrangian approach. The Eulerian approach to the gas-phase flow was based on solving the fluid flow conservation equations, closed using a second-moment turbulence closure. The trajectories and velocities of solid particles were simulated using a three-dimensional Lagrangian particle tracking approach under the assumption of one-way coupling between the gas and particle phases, coupled to a three-dimensional particle-wall interaction algorithm, with a random Fourier series method used to derive instantaneous velocities from the time-averaged Eulerian solutions. The performance of the overall model was tested for a gas-solid flow in a horizontal-to-vertical duct, with predictions for both phases showing good agreement with experimental data.

The streamwise velocity within the bend section was found to be influenced by strong pressure gradients near the convex and concave walls, the cross-stream flow induced in the cross-section of the bend, and centrifugal forces acting on the fluid. Just upstream of the bend in the horizontal section of the duct, the flow is accelerated in regions near the inner-radius wall, due to the favorable pressure gradient in the direction of the flow. In contrast, the flow is decelerated in regions near the outer-radius wall due to the developed adverse pressure gradient within the bend. Downstream of the bend, in the vertical section of the duct, the maximum streamwise velocity is shifted toward the outer wall owing to the centrifugal effect. Further

downstream the fluid recovers, although the influence of the bend persists to large distances.

The particulate flow was influenced by the instantaneous gas-phase flow, the particle-size distribution, and particle-wall collisions. Small particles, having a small relaxation time and, hence, a low-Stokes number, followed the gas streamlines, with an even distribution over the entire cross-section of the duct. Larger particles, with high-inertia and Stokes numbers, were driven toward the outer wall of the duct due to the effects of inertia and gravity, leading to a gradient in their distribution across the duct and the phenomena of particle roping. These particles also frequently collided with the outer wall of the duct. Two-way or four-way coupling might be used in the future to more accurately resolve fluid-particle momentum transfer in regions where the particle roping phenomena occurred.

Overall, the present results compare favorably with those of other authors[4,6,7,32] who predicted the same flow, most notably in providing reasonable predictions of the rms of the particle velocity fluctuation in the streamwise direction. Differences between the present work and that of the authors noted lie in the consistent application, herein, of an anisotropic approach in predictions of both the time-averaged turbulent velocities in the RANS model and instantaneous velocities by the dispersion model. The other notable difference between the present and previous work is in the use in this study of three dimensional simulations of both the gas and particle phases, which ensures that particle cross-stream trajectories, particularly relevant for particles with low-Stokes numbers, are considered and their impact on the resulting streamwise fluctuating particle velocities accommodated. Finally, the present work employed much larger numbers of particles in the simulations compared to previous works, although this is to be expected given the use of fully three-dimensional calculations. It is worthy of note, however, that the dispersion model used does not accommodate the influence of off-diagonal components of the fluid Reynolds stress tensor, and the use of more elaborate approaches,[33–35] which use spatial, temporal, and directional correlations of the Reynolds stresses seen by the particle to give values for the fluctuating fluid velocities, is worthy of further investigation.

Acknowledgments

The authors thank the Commonwealth Scholarship and Fellowship Plan (CSFP) United Kingdom for supporting D.O. Njobuenwu's research.

Notation

A_{ij} = redistributive fluctuating pressure term
$C_{1\text{-}5}, C_s, C_\varepsilon, C_{\varepsilon 1}, C_{\varepsilon 2}$ = turbulence model constants
C_D = particle drag coefficient
C_P = pressure coefficient
C_{Sl} = slip shear lift coefficient
C_μ = constant in Prandtl-Kolmogorov relationship
d_p = particle diameter
D = duct side length
e = coefficient of restitution
E = turbulence energy spectrum
f_D = drag factor
F = forces acting on particles
g = gravitational acceleration
I = turbulence intensity
k = turbulence kinetic energy
l = characteristics length scale of turbulence
L = mass loading
m = mass
n = number of particle tracks
N_p = number of particles
P = static pressure
r = radial direction
r_i = inner wall radius
r_o = outer wall radius
r^* = nondimensional wall distance
R = bend radius
R_r = bend radius to duct diameter ratio
Re = Reynolds number
Re_p = particle Reynolds number
S = distance along straight section of duct
St = particle Stokes number
t = time
u,v,w = velocities in x, y, z direction
$u_{p,n}$ = particle normal velocity
$u_{p,t}$ = particle tangential velocity
U_m, V_m, W_m = amplitudes of fluctuation
W_b = bulk gas velocity
x,y,z = Cartesian co-ordinates corresponding to transverse, spanwise and streamwise directions

Greek letters

α_p = particle volume fraction
α^u, α^v, α^w = initial phase angle of fluctuation in transverse, spanwise and streamwise directions
β = ratio of shear flow Reynolds number and particle Reynolds number
γ = normally distributed random number
ε = turbulence kinetic energy dissipation rate
δ_{ij} = Kronecker delta
$\Delta\gamma$ = roughness angle of collision
Δt = time step
θ = bend angle
θ, θ' = particle incident angle without and with roughness effect
μ = dynamic viscosity
μ = kinematic viscosity
ξ = Gaussian random number with zero mean and standard deviation of unity
ξ_p = particle number flow rate per particle track
ρ = density
τ = dummy time variable
φ = arbitrary variable
ω = frequency of fluctuation
ω_f, ω_p = fluid and particle rotation

Subscripts

b = bulk average air velocity in duct
B = buoyancy
cv = control volume
D = drag
e = eddy lifetime
g = gravity
i = ith particle
in = inlet value
i,j,k = i, j, k direction
max = maximum value
n = normal direction
o = outer
p = dispersed particle phase
P = pressure
r = eddy transit time
Sl = slip shear lift

t = tangential direction
x,y,z = Cartesian co-ordinates

Superscripts

0 = Initial or upstream value
1 = before
2 = after
$\bar{}$ = Reynolds average
$'$ = fluctuating component
$''$ = rms of fluctuating velocity
$\vec{}$ = vector

Literature Cited

1. Iacovides H, Launder BE, Loizou PA. Numerical computation of turbulent flow through a square-sectioned 90-degrees bend. *Int J Heat Fluid Flow*. 1987;8:320–325.
2. Raisee M, Alemi H, Iacovides H. Prediction of developing turbulent flow in 90 degrees-curved ducts using linear and non-linear low-Re k-epsilon models. *Int J Numer Methods Fluids*. 2006; 51:1379–1405.
3. Quek TY, Wang C-H, Ray MB. Dilute gas-solid flows in horizontal and vertical bends. *Ind Eng Chem Res*. 2005;44:2301–2315.
4. Mohanarangam K, Tian ZF, Tu JY. Numerical computation of turbulent gas-particle flow in a 90 degree bend: comparison of two particle modelling approaches. *ANZIAM J*. 2007;48:C741–C758.
5. Kliafas Y, Holt M. LDV measurements of a turbulent air-solid two-phase flow in a 90° bend. *Exp Fluids*. 1987;5:73–85.
6. Kuan B, William Y, Solnordal C. CFD simulation and experimental validation of dilute particulate turbulent flow in 90° duct bend. 3rd International Conference on CFD in the Minerals and Process Industries, CSIRO. Melbourne, Australia, 2003:531–536.
7. Kuan B, Yang W, Schwarz MP. Dilute gas-solid two-phase flows in a curved 90° duct bend: CFD simulation with experimental validation. *Chem Eng Sci*. 2007;62:2068–2088.
8. Yang W, Kuan B. Experimental investigation of dilute turbulent particulate flow inside a curved 90° bend. *Chem Eng Sci*. 2006; 61:3593–3601.
9. Gosman AD, Ioannides E. Aspects of computer simulation of liquid-fuelled combustors. AIAA-81–0323, AIAA 19th Aerospace Sciences Meeting. St. Louis, MO, 1981.
10. Tian ZF, Inthavong K, Tu JY, Yeoh GH. Numerical investigation into the effects of wall roughness on a gas-particle flow in a 90° bend. *Int J Heat Mass Transfer*. 2008;51:1238–1250.
11. Sommerfeld M, Huber N. Experimental analysis and modelling of particle-wall collisions. *Int J Multiphase Flow*. 1999;25:1457–1489.
12. Yilmaz A, Levy EK. Formation and dispersion of ropes in pneumatic conveying. *Powder Technol*. 2001;114:168–185.
13. Yilmaz A, Levy EK. Roping phenomena in pulverized coal conveying lines. *Powder Technol*. 1998;95:43–48.
14. Fokeer S, Kingman S, Lowndes I, Reynolds A. Characterisation of the cross sectional particle concentration distribution in horizontal dilute flow conveying - a review. *Chem Eng Process*. 2004;43:677–691.
15. Fan JR, Zhang XY, Chen LH, Cen KF. New stochastic particle dispersion modeling of a turbulent particle-laden round jet. *Chem Eng J*. 1997;66:207–215.
16. Fan JR, Zhang XY, Cheng LH, Cen KF. Numerical simulation and experimental study of two-phase flow in a vertical pipe. *Aerosol Sci Technol*. 1997;27:281–292.
17. Fan JR, Yao J, Cen KF. Antierosion in a 90 degrees bend by particle impaction. *AlChE J*. 2002;48:1401–1412.
18. Jones WP, Musonge P. Closure of the Reynolds stress and scalar flux equations. *Phys Fluids*. 1988;31:3589–3604.
19. Dianat M, Fairweather M, Jones WP. Reynolds stress closure applied to axisymmetric, impinging turbulent jets. *Theor Comput Fluid Dyn*. 1996;8:435–447.
20. Rhea S, Bini M, Fairweather M, Jones WP. RANS modelling and LES of a single-phase, impinging plane jet. *Comput Chem Eng*. 2009;33:1344–1353.
21. Jones WP. *BOFFIN: a computer program for flow and combustion in complex geometries*. London, UK: Department of Mechanical Engineering, Imperial College of Science, Technology and Medicine; 1991.
22. Brenn G, Braeske H, Zivkovic G, Durst F. Experimental and numerical investigation of liquid channel flows with dispersed gas and solid particles. *Int J Multiphase Flow*. 2003;29:219–247.
23. Mei R. An approximate expression for the shear lift force on a spherical particle at finite Reynolds number. *Int. J. Multiphase Flow*. 1992;18:145–147.
24. Shirolkar JS, Coimbra CFM, McQuay MQ. Fundamental aspects of modeling turbulent particle dispersion in dilute flows. *Prog Energy Combust Sci*. 1996;22:363–399.
25. Sommerfeld M. Modelling of particle-wall collisions in confined gas-particle flows. *Int J Multiphase Flow*. 1992;18:905–926.
26. Naik S, Bryden IG. Prediction of turbulent gas-solids flow in curved ducts using the Eulerian-Lagrangian method. *Int J Numer Methods Fluids*. 1999;31:579–600.
27. Laurence JC. Intensity, scale, and spectra of turbulence in mixing region of free subsonic jet: NACA Report No. 1292; 1956.
28. Grant G, Tabakoff W. Erosion prediction in turbomachinery resulting from environmental solid particles. *J. Aircraft*. 1975;12:471–478.
29. Tsai SF, Sheu TWH. Numerical exploration of flow topology and vortex stability in a curved duct. *Int. J. Numer. Methods Eng*. 2007;71:564–582.
30. Sudo K, Sumida M, Hibara H. Experimental investigation on turbulent flow in a square-sectioned 90-degree bend. *Exp. Fluids*. 2001;30:246–252.
31. Tu JY, Fletcher CAJ. Numerical computation of turbulent gas-solid particle flow in a 90-degrees bend. *AlChE J*. 1995;41:2187–2197.
32. Ibrahim KA, El-Kadi MA, Hamed MH, El-Behery SM. Gas-solid two-phase flow in 90° bend. *Alexandria Eng. J*. 2006;45:417–433.
33. Berlemont A, Desjonqueres P, Gouesbet G. Particle Lagrangian simulation in turbulent flows. *Int J Multiphase Flow*. 1990;16:19–34.
34. Burry D, Bergeles G. Dispersion of particles in anisotropic turbulent flows. *Int J Multiphase Flow*. 1993;19:651–664.
35. Zhou Q, Leschziner MA. *A time-correlated stochastic model for particle dispersion in anisotropic turbulence*. 8th Symposium on Turbulent Shear Flows. Munich, Germany, 1991; 1:10-3-1 to 10-3-6.

Manuscript received July 22, 2010, and revision received Dec. 20, 2010.